5-8-2017

Hemispherical Grid Retarding Field Analyzer Redesign for Secondary Electron Emission Studies

Greg Wilson
Utah State University

JR Dennison
Utah State Univesity

Recommended Citation

UtahState University
MERRILL-CAZIER LIBRARY

Hemispherical Grid Retarding Field Analyzer Redesign for Secondary Electron Emission Studies

Gregory Wilson

Abstract—**A redesign of the Hemispherical Grid Retarding Field Analyzer is discussed in relationship to multilayer charging models. In order to accurately extend single layer charging models to dynamic multilayer scenarios, precise measurements of electron emission as well as the net surface potential must be made. By learning from the previous design and thinking of future applications, the new instrument will greatly enhance our ability to precisely measure materials undergoing energetic electron bombardment.**

Keywords—Electron emission, energetic electron bombardment, multilayer materials, surface potential, 3D modeling

I. INTRODUCTION

The charging of multilayer materials as related to the charging of spacecraft is one of the primary concerns related to spacecraft in the space environment. To understand how electron bombardment effects multilayer materials, an in depth study of energy dependent material properties must be undertaken. These properties include the electron penetration depth, secondary electron emission, charge transport and electrostatic discharge. By using energy dependent models of these properties, along with the geometry of the system, multilayer models can be developed to predict the time evolution of the internal charge distribution. Using these models, the net surface potential and the measurement of electrode currents can be used to extrapolate information about the internal charge distribution.

One of the greatest difficulties in making these measurements is the instrumentation itself. USU's Materials Physics Group has spent over a decade designing and building instrumentation for materials testing with a focus on the space environment. By understanding the issues and complications of the past and looking forward to future applications, a new instrument is being designed which will further our ability to accurately measure the effects of electron bombardment on conductive and insulating materials. This will allow for more accurate models and better predictions to be developed.

II. THEORETICAL BACKGROUND

When an energetic electron interacts with a material, several energy dependent phenomena must be considered. The first, the electron range determines the depth at which a charge layer is deposited [2]–[4]. The range will also determine whether or not the beam is penetrating or non-penetrating. Equally important is the total electron yield - defined as the

Gregory Wilson is with the Materials Physics Group in the Physics Department at Utah State University in Logan, UT 84322 USA (e-mail: gregdwilson@gmail.com)
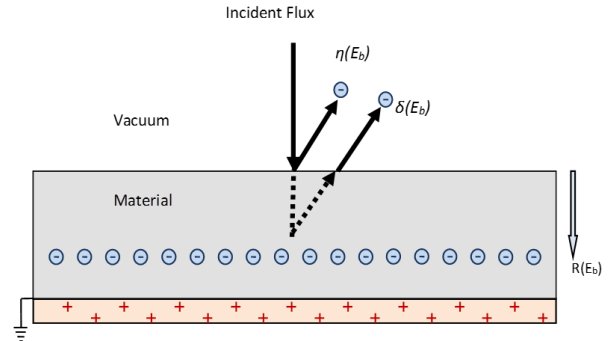

Fig. 1. Diagram of incident electron flux impinging on a generic material. $\eta(E_b)$ denotes the backscattered yield for electrons that originate within the incident beam or that have emission energies E>50 eV. $\delta(E_b)$ denotes the secondary yield for electrons liberated from within the material or that have emission energies E<50 eV. The total yield for all emission energies is the sum of the secondary and backscattered yield; $\sigma(E_b) = \eta(E_b) + \delta(E_b)$. $R(E_b)$ is the incident energy-dependant electron penetration depth (range) [1], [2].

number of electrons ejected from the surface of the material versus the number of electrons incident on the material - which determines the surface charge layer [4]–[6]. The static conductivity also contributes to the internal charge evolution, but it is not highly dependent upon the energy of the incoming electrons [7], [8]. However, energy-dependent radiation induced conductivity must be take into account for high electron fluxes [9], [10].

Using these models, coupled with measurement of the net electrode currents as well as the net surface potential, allow an in depth study of a material and its behavior in various charging scenarios.

A. Electron Range

The range, R, or maximum distance an electron of a given incident energy can penetrate through a material before all kinetic energy is dissipated and the electron comes to rest, is a common way to parameterize electron interactions with materials. The range is used in spacecraft charging calculations to predict the charge distribution of deposited electrons in materials and to model secondary and backscattered electron emission. It is also used to predict the distribution of energy deposited by incident electrons as they traverse a material [1], [11]; this distribution is further used to model radiation induced conductivity and cathodoluminescence.

It is therefore important for spacecraft charging models to have a realistic, reasonably accurate, and efficient expression to predict the approximate range of electron energies commonly encountered in space plasma fluxes, from ~10 eV to ~10 MeV. Detailed expressions for the range have been developed starting from early work by Bethe [12]; however, these models often have restricted energy ranges of applicability and involve many fitting parameters. A simple single-parameter approximation has been developed that can be readily implemented for a wide array of conducting, semiconducting and insulating spacecraft materials with a minimal number of fitting parameters based on a constant rate of energy deposition with depth referred to as the continuous slow down approximation (CSDA) [2], [3].

The Materials Physic Group has developed composite analytic approximation to the range, spanning incident energies from <10 eV to >100 MeV, with a single fitting parameter, N_v^{eff} [2], [3]:

$$R\left(E_b; N_v^{eff}\right) =$$
$$\begin{cases} \left[\frac{E_b}{\bar{E}}\right]\left[\lambda_{\text{IMFP}}\left(\bar{E}\right)\frac{\left(1-e^{-\bar{E}/\bar{E}}\right)}{\left(1-e^{-E_b/\bar{E}}\right)}\right]\left(1-e^{-E_b/\bar{E}}\right)^{-1} \\ \qquad\qquad\qquad \text{if } E_b < \bar{E} \\ \left[\frac{E_b}{\bar{E}}\right]\lambda_{\text{IMFP}}\left(E_b\right)\left(1-e^{-E_b/\bar{E}}\right)^{-1} \\ \qquad\qquad\qquad \text{if } \bar{E} \leq E_b \leq E_{\text{HI}} \\ b\, E_b^n\left[1-\left[1+\left(\frac{E_b/N_v^{eff}}{m_e\, c^2}\right)\right]^{-2}\right] \\ \qquad\qquad\qquad \text{if } E_b > E_{\text{HI}} \end{cases}$$
(1)

B. Electron Yield

As energetic electrons interact with the surface of materials, they impart energy throughout the material, as described by the range process. If the energy exchange is near the surface, electrons in the material can be excited and emitted. It is also possible for the incident electron to undergo a quasi-elastic collision near the surface, wherein the electron is backscattered from the surface and therefore imparts no charge to the material. This process of electron emission from the surface, known as the electron yield, is highly dependent upon the incident electron energy. The total electron yield, defined as the ratio of emitted to incident flux is fundamental in understanding the charging of materials [1].

The incident flux is the total number of electrons entering the material from the environment. The incident flux in a space environment consists of a distribution of energetic electrons at different energies and different incident angles. The proposed studies use a monoenergetic beam of electrons normally incident upon the surface of the material. This allows the models to be simplified in order to understand the fundamental principles which drive the charging process.

The emitted flux is the sum of backscattered and secondary electrons, as shown in Fig. 1. Secondary electrons, which originate within the material, conventionally have energies <50 eV where backscattered electrons, which originate from the incident beam, conventionally have energies >50 eV; where
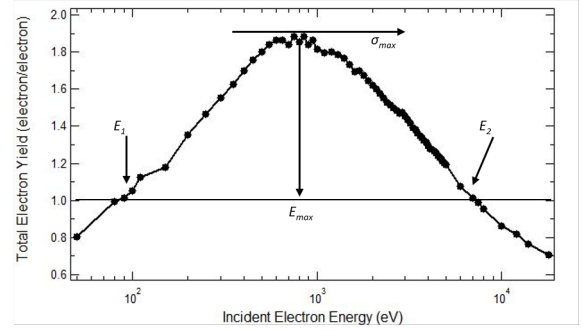

Fig. 2. Total electron yield of polycrystalline Au as a function of incident energy. Data were taken using a DC electron beam. E_1 and E_2 are the first and second crossover energies where yield with $\sigma > 1$ occur when $E_1 < E_b < E_2$. The yield peak, σ_{max}, is the maximum yield and occurs between the crossover energies at E_{max}. (Hoffmann, 2010)

the secondary yield is then defined as the ratio of secondary electrons to the incident electrons, denoted as $\delta(E_B)$, whereas the backscattered yield is the ratio of backscattered electrons to incident electrons denoted as $\eta(E_b)$ where E_b is the electron beam energy. Thus the total electron yield is the sum of these two, given by $\sigma(E_b) = \eta(E_b) + \delta(E_b)$.

The yield, as shown in Fig. 2, is highly energy dependent with "crossover" energies at E_1 and E_2 and a maximum yield σ_{max} at E_{max}. At very low energies, electrons generally do not have enough energy to excite many electrons, thus low energy electrons generally produce yields less than one. As the energy increases, the probability of multiple collisions near the surface increases which causes the yield to rise above one. As the energy increases, the electron inelastic mean free path increases causing the collision to occur deeper within the material, decreasing the likelihood of the electron reaching and escaping the surface; this leads to a decrease in σ above E_{max}

As with the range, the yield is actually a function of the "landing energy" $[E_b+q_eV_s]$ rather than E_b. Dynamic emission models provide models for yield as a function of surface voltage, V_s or charging. A simple model for surface voltage (or time) dependence of the yield for negative charging for $E_b > E_2$, based on a charging capacitor, was proposed by Thomson [11]:

$$[1 - Y(t; E_b + q_eV_s)] = [1 - Y(E_b + q_eV_s)]\, e^{-Q(t)/\tau_Q}$$
(2)

for $0 \geq q_eV_s(t) \geq (E_2 - E_b)$, τ_q is a decay constant for the exponential approach of the yield to unity, as charge $Q(t)$ is accumulated with elapsed time, E_2 is the crossover energy and Y is the yield. A more in depth discussion is given by Hoffmann [5].

C. Conductivity

The conductivity of a material determines how easily a deposited charge layer can move through the material in response to an electric field, $J(t) = \sigma(t)F(t)$; each term can be time-dependant. These electric fields, F, are produced by
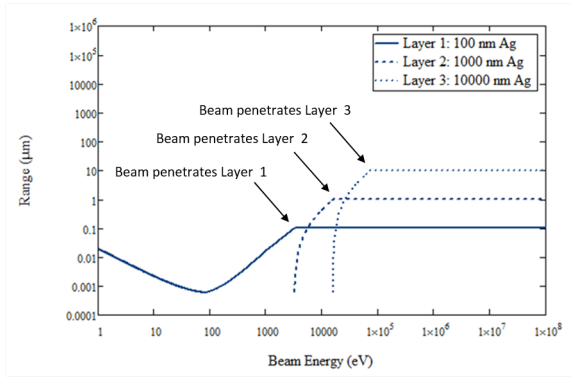
Fig. 3.   Estimated range for three layers of Ag. The flat regions are when the beam penetrates that layer.

the embedded charge layers, the depletion layer, and grounded conductors in the material. The measured currents will have two terms, a particle current conductivity proportional to the conductivity and a displacement current due to the change in the electric field due to charge accumulation and mitigation.

For conditions considered here, we assume the conductivity has only two terms, the equilibrium (dark current) conductivity and radiation induce conductivity; we neglect contributions for polarization, diffusion and dispersion based on arguments related to the time dependence of these contributions compared with our experimental times [13], [14]. For low electron fluxes the conductivity, $\sigma(t)$, is a static conductivity that approaches the equilibrium (dark current) conductivity of the material, σ_{DC}.

III.   MULTILAYER INTERACTIONS

Many materials used in spacecraft charging are not a single layer. Because of this, multilayer models need to be developed in order to help determine the effects of the space environment on these materials. This section will again discuss the fundamental processes in spacecraft charging, but with regards to multilayer materials. We will again start with the electron range, and then discuss the electron yield and conductivity.

A. Multilayer Electron Range

Knowing the range of electrons becomes especially critical when dealing with multilayer materials, where the incident energy will determine where and in what layer charge and energy are deposited. Since the electron range is dependent upon the incident beam energy, for subsequent layers, the beam energy must be scaled to account for the energy lost in any proceeding layers. To scale the energy, we can assume a constant energy loss with penetration distance (constant stopping power), as is done in the continuous slow down approximation (CSDA) of the range. Thus, the incident energy can be calculated for a second layer by

$$E_{\text{Layer2}} = E_b \left(1 - \frac{d_{\text{Layer1}}}{R_{\text{Layer1}}(E_b)} \right), \tag{3}$$

where E_{Layer2} is the energy of electrons entering the second layer, d_{Layer1} is the thickness of the first layer and $R_{\text{Layer1}}(E_b) > d_{\text{Layer1}}$ is the range in the first layer as a function of the beam energy. The range for the second layer is then given by $R_{\text{Layer2}}(E_{\text{Layer2}})$. For a third layer we can once again scale the energy and calculate the range. Thus the incident electron energy for the subsequent j^{th} layer is given by

$$E_{\text{Layer}(j)} = E_{\text{Layer}(j-1)} \left(1 - \frac{d_{\text{Layer}(j-1)}}{R_{\text{Layer}(j-1)}\left(E_{\text{Layer}(j-1)}\right)} \right), \tag{4}$$

where $E_{\text{Layer}(j)}$ is the energy of electron entering the jth layer, $d_{\text{Layer}(j-1)}$ is the thickness of the $j-1$ layer and the electron range given by $R_{\text{Layer}(j)}(E_{\text{Layer}(j)})$. A comparison of Ag in three different layer configurations is given in Fig 3.

B. Multilayer Electron Yield

The electron yield of multilayer materials is largely driven by the range of the excited secondary electrons in the material. Because secondary electrons by conventional definition have energies <50 eV, those at a depth greater than the range are not able to escape the material. Thus, if the first layer is thicker than the range of secondary electrons, the secondary electron yield will be driven by the top layer. As the top layer becomes sufficiently thin, such as a thin contamination layer, the secondary electron yield approaches that of the bulk material. This is seen in the approximation for the total electron yield for contamination layers proposed by Davies, Dennison and Chang [15], [16] where the time evolution of the secondary electron yield δ_{tot} for a bulk layer δ_B and a surface contamination layer δ_S is given by

$$\delta_{\text{tot}}(t) = \delta_B e^{-\gamma t} + \delta_S \left(1 - e^{-\gamma t} \right) \tag{5}$$

where δ_B is the yield of the bulk material, δ_S is the yield of the surface material and $\gamma \equiv dz/dt$ is the growth rate of the contamination layer. Thus, given that the contamination layer grows at a rate of $z = \gamma t$, we can make the conversion from time dependence to depth dependence by substituting z for γt. Thus, our equation becomes

$$\delta_{\text{tot}}(z) = \begin{cases} \delta_S & R_{\max}(E_{\text{SE}}) < z \\ \delta_B & R(E_b) < z) \\ \delta_B e^{-z} + \delta_S(1 - e^{-z}) & \text{otherwise} \end{cases} \tag{6}$$

where $R_{\max}(E_{\text{SE}})$ is the maximum range in the top layer for secondary electrons.

C. Multilayer Conductivity

The conductivity of multilayered materials is dependent upon the individual layer conductivity as well as the layer configuration. For a composite material consisting of two parallel layered materials as shown in Fig. 4 the total conductivity and resistivity of the material are given by

$$\frac{1}{\sigma_{\text{tot}}} = \frac{1}{\sigma_1} + \frac{1}{\sigma_2} = \rho_1 + \rho_2 = \rho_{\text{tot}}, \tag{7}$$
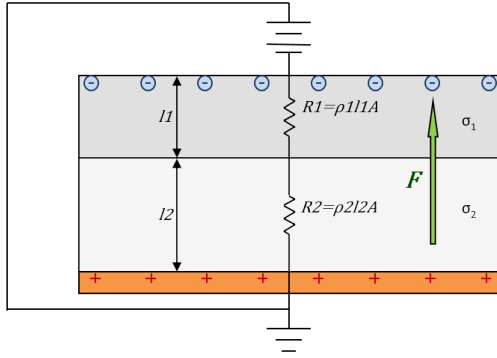
Fig. 4.   The total conductivity of a dual layer material is given by Eq. 7. The total resistance is dependent upon the layer thickness, as well as the depth at which the charge layer is deposited.

Fig. 5.   Cross section diagram for original HGRFA.

where $\sigma_{1,2}$ are the conductivities and $\rho_{1,2}$ are the resistivities of the first and second layer, respectively. The total resistance is given by

$$R_{\text{tot}} = R_1 + R_2 = \frac{\rho_1 l_1 + \rho_2 l_2}{A}, \qquad (8)$$

where $l_{1,2}$ are the thickness of layer 1 and 2, respectively, and A is the cross sectional area. Since the charge layers are often not at the surface, such as an embedded charge from an electron beam at depth $R(E_b)$ [17], then the length l becomes $l - R(E_b)$. Thus, for an embedded charge layer in the top layer at a distance $R(E_b)$ the total resistance is given by

$$R_{\text{tot}} = \frac{\rho_1 \left(l_1 - R\left(E_b \right) \right) + \rho_2 l_2}{A}. \qquad (9)$$

In many cases, a conductive layer is placed in between two dielectrics; see, for example, the study by Wilson [18]. In this scenario, if there exists an ungrounded conductive layer between the two layers, the conductive layer acts as a direct connection between the two layers like a wire in a dual resistor circuit and makes no change to the total resistance. It may however, change the depth at which the electron beam penetrates. The picture is more complicated if the conductive layer is grounded, allowing charge to flow into the conductor from ground [18], [19]

Another composite material configuration consists of parallel layers forming vertical columns of materials which can be modeled similarly by parallel resistor circuits. This model can then be extended surface roughness models with one of the materials consisting of vacuum.

IV.   CURRENT INSTRUMENTATION

USU's MPG has previously developed instrumentation which enables the characterization and measurement of materials undergoing energetic electron bombardment. This instrumentation consists of an ultrahigh vacuum chamber equipped with electron guns, a sample carousel, temperature controllers, electrical feedthroughs, a surface voltage probe (SVP), a hemispherical grid retarding field analyzer (HGRFA) and other
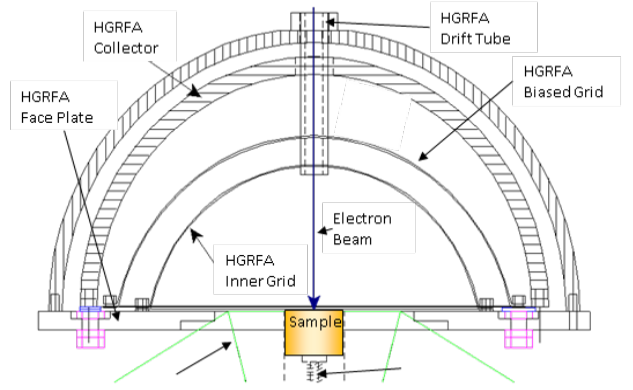
various instrumentation. This chamber is equipped to simulate diverse space environments from 10^{-10} to 10^{-3} Torr and electron fluxes with energies from 10 to 30,000 eV.

The HGRFA and the SVP are the primary instruments that will be used in the studies outlined in Section II and are the focus of design improvements in Section V. The HGRFA is an detector used to measure electron emission from insulators and conductors undergoing electron bombardment. The original design is shown in Fig. 5. It can also be used for stimulated emission studies. It was originally developed by Nikels [20] and Thomson [11] and then further improved by Hoffmann [1] and Christensen [21].

The HGRFA fully encloses one of eleven samples that can be positioned in front on a charged particle source via rotation of the sample carousel. An aperture on the front of the instrument allows an incoming electron or ion beam to bombard the sample. A enclosing hemisphere allows the capture of all emitted electrons with a retarding-field analyzer grid system for emitted-electron energy discrimination. The current instrument was originally calibrated giving yield accuracies with systematic errors $< 5\%$ [1]. It was then further improved by Christensen, wherein he reduced electrical noise, reduced sample charging, improved charge neutralization and improved analysis methods [21].

The SVP, originally built and validated by Hodges [14], is used to measure the net surface potential of charged insulators. It uses a capacitive technique employing two electrically connected Au plates, one inside the chamber and one outside the chamber. By measuring the potential on the outside plate using an electrostatic field probe and moving the inside plate over the sample, the net surface potential of the sample can be calculated given the system is properly calibrated. This system was originally purposed to work in conjunction with the HGFRA; however, due to equipment failure and other complications this was never fully realized.

V.   DESIGN IMPROVEMENTS

In order to fully develop and validate the multilayer charging models, several instrument upgrades must be carried out. The original plan was to modify the existing HGFRA; however,
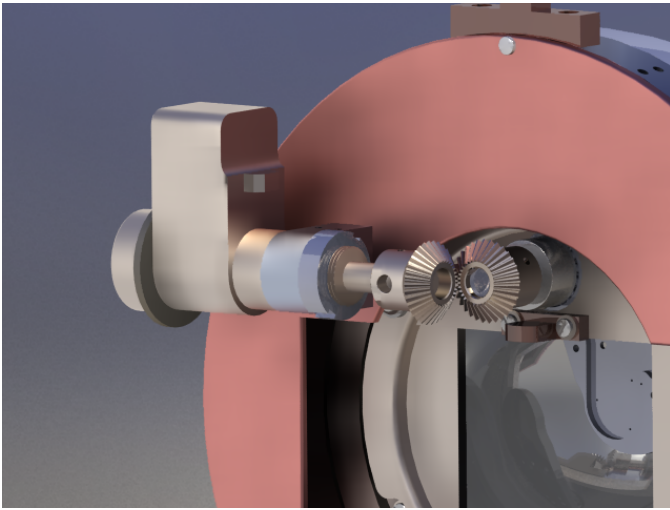
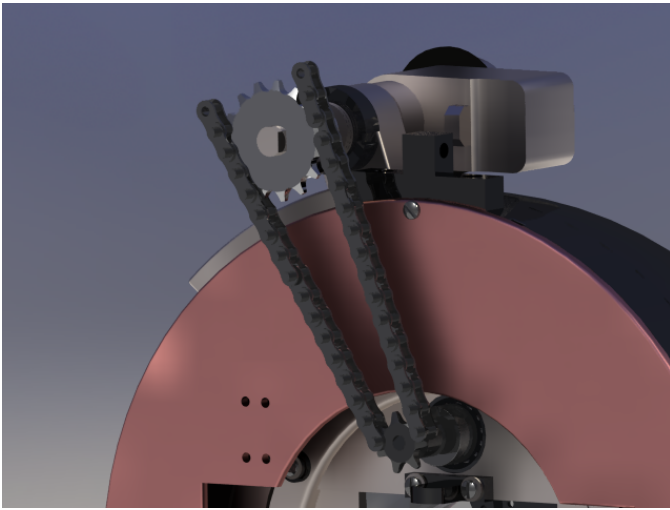Fig. 6. Miter gear drive design for the SVP motor mount.

Fig. 8. Collapsed view of the HGRFA to show isolated rings with attached hemispheres.

Fig. 7. Chain drive design for the SVP motor mount.

Fig. 9. Exploded view of the HGRFA to show isolated rings with attached hemispheres.

after consideration it was concluded that this was not feasible nor would it achieve the necessary requirements. Because of this a new re-design of the HGFRA was completed, which incorporated the necessary upgrades. The design changes can be grouped into several categories which include; Surface Voltage Probe, Electrically Isolated Rings Design, Front Instrument Plate, Hemispheres, Wiring, and Center Rod Alignment.

A. Surface Voltage Probe

The primary reason for the re-design of the HGRFA was to incorporate the SVP with the HGRFA. The original complications arose due to the inability to repair the damaged stepper motor. The replacement motor was not only larger then the original, but it also had a different form factor. To overcome this, two solutions were designed as shown in Figs. 6 and 7. The first solution uses a set of miter gears which allows the
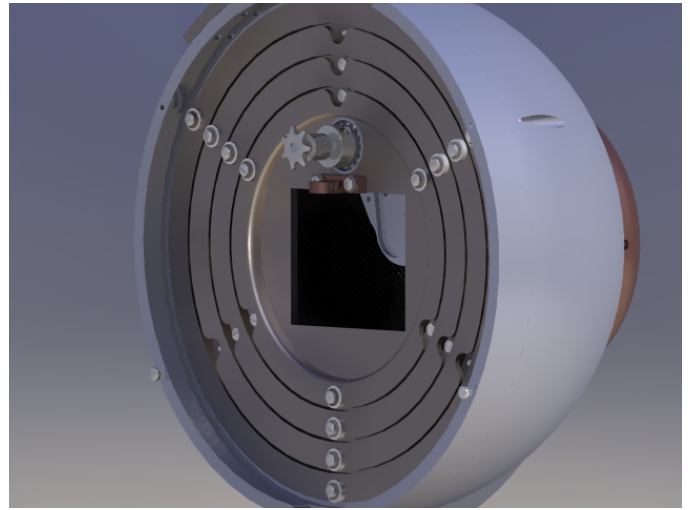
motor to be mounted sideways and the second uses a precision gearing system with a miniature chain. The second method allows the motor to be positioned on the top of the device allowing greater flexibility in motor choice.

Incorporating the SVP with the HGRFA facilitates several capabilities. The first capability includes the ability to measure the charge deposited in multilayer materials. This is done by first measuring the current coming into the sample and the current leaving the sample, either by electron emission or by conductance, as well as any image currents. The net surface potential is then measured, which together with the measured currents, can help determine in which layers the charge was deposited.

The second application deals with the charging of insulators during secondary electron emission studies. As the secondary
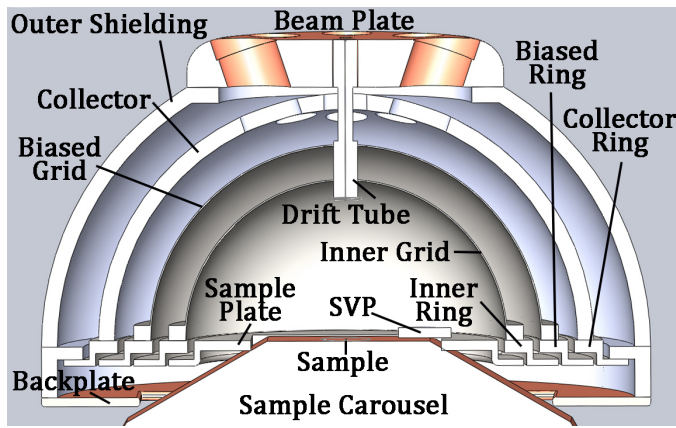
Fig. 10. Cross section of the HGRFA to show isolated rings, the inner and biased grids, the collectors, the drift tube and the beam plate. This also shows how the instrument is designed to allow the sample carousel to recess within the instrument to allow the sample to align flush with the sample plate.

Fig. 11. Front view of the HGRFA to show the front instrument plate design as well as the wire housing.

electron emission of insulators are being measured, they can charge positively or negatively. For low energy electron beams this becomes increasingly important since the charging of the sample not only changes the electron landing energy but it also creates an electric fields within the HGRFA. In order to negate this, the stage and the inner grid can be biased to match the potential of the sample; however, to do this, the potential must first be known. By making repeated measurements of the sample using the SVP during measurments, the bias required can be continually updated as the sample charges. By using this method the true intrinsic yield of highly insulating materials can be extracted.

Other applications that require both the HGRFA and the SVP include charge buildup effects on cathodoluminescence, charge buildup effects on arcing, as well as charge accumulation and decay for highly insulated materials undergoing electron bombardment. All of these measurements require that both the HGRFA and the SVP are working in conjunction with one another.

B. Electrically Isolated Rings Design

In order to increase the reliability of the instrument and to ease assembly and disassembly, the grids were re-designed to attach to electrically isolated rings, which connect to form the back plate of the device as shown in Fig. 8. Figure 9 shows the an exploded view of the HGRFA with the grids and collector attached to the isolated rings. This not only makes them more reliable and easier to assemble and disassemble, it also isolates the outer shielding from the stage and creates the possibility to have modular sample plates for various mounting configurations.

The reliability of the design comes from the ability to mount the hemispherical grids, as well as the collector, directly to their respective rings. This allows each grid to be independently assembled and disassembled allowing each grid to be removed and repaired without disassembling the entire instrument. This also allows the electrical connections to be
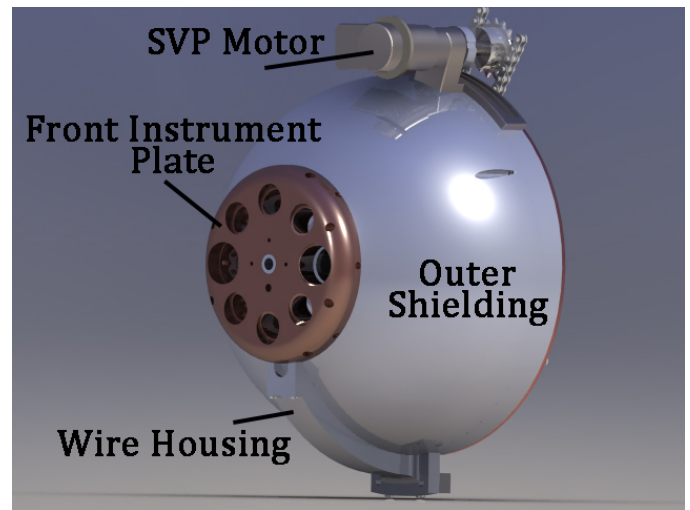
made to each ring independently which makes wiring more versatile and robust.

Another feature that this design offers is the ability to isolate the inner plate, which electrically connects to the stage, with the outer shielding and beam aperture. This enables the current from the stage to be used to help determine the total emitted current from the sample, since the stage is part of the enclosing hemisphere.

This modular ring design also allows for the design of different sample plates for different mounting configurations. This includes the mounting to a separate thermally controlled sample stage with temperatures ranging from 40 K to 293 K [22]. It also includes the ability to attach it in a horizontal configuration which would allow loose dust and powders to be measured.

The rings are then shielded with a copper backplate as shown in Figs. 10 and 12, which reduces noise and protects the rings and wiring from other conductors. The rectangle cutout allows for the sample carousel to fit flush against the sample plate, as shown in Fig. 10.

C. Front Instrument Plate

The original front instrument panel had several modifications to it, however, these caused several issues. One of the greatest issues is that the instrument ports do not have a clear view of the sample due to the drift tube. This creates shadows on the sample from the UV light source as well as the electron flood gun. In order to rectify this issue, the new front instrument panel will have the instrument ports placed at large angles from the drift tube, so that they have a clear view of the sample. This will also reduce the number of emitted electrons that escape through the opening in the collector since emission falls off as a function of $\cos(\theta)$ or faster [1].

The new design as shown in Fig. 11, will also enable the entire front instrument panel to be easily removed and replaced
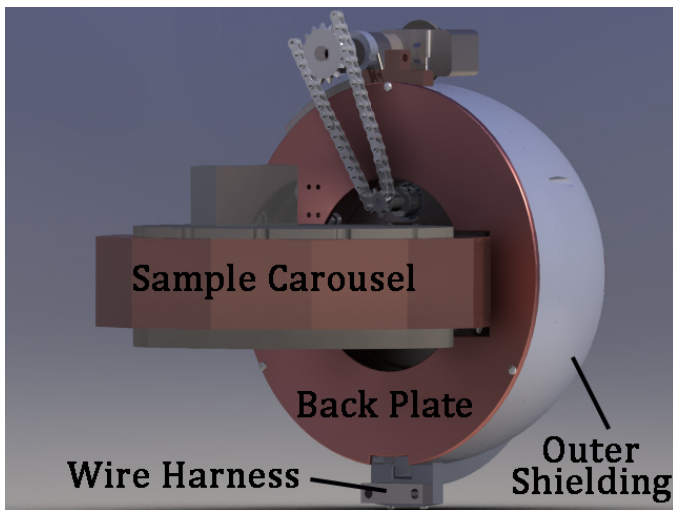
Fig. 12. Back view of the HGRFA to show the backplate as well as how the carousel will align in relation to the HGRFA.
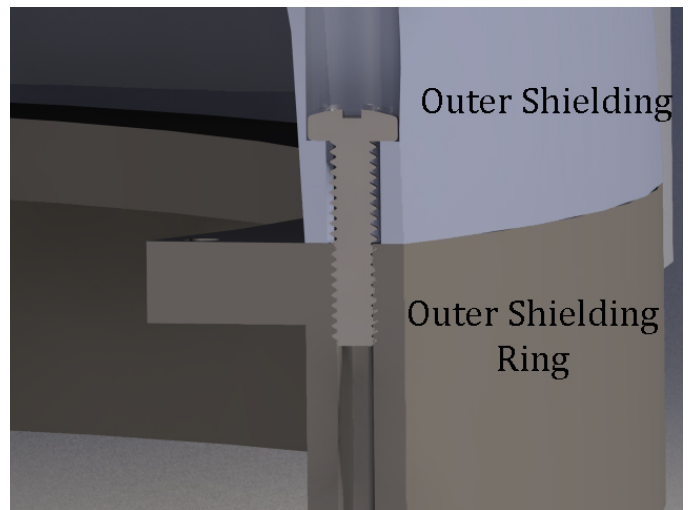

Fig. 13. Cross section view of the HGRFA outer shielding and outer shielding ring. With this design the outer shield hemisphere will be protected from bulging and stripping in contrast with Fig. 14

if necessary. This allows the instrument to be modified without needing to redesign the entire outer-shielding

D. Hemispheres

When the original instrument was being designed there was no cost effective way to manufacture custom hemispheres to be used as grid mandrels. Because of this, compromises were made wherein already manufactured hemispheres were purchased. These hemispheres, however, were slightly aspherical. Because the grids are formed by laying wire mesh over one of these hemispheres, any asphericity was also transfered to the grids. Because of this, the electric fields between the biased grid and the inner grid and the biased grid and the collector were not purely radial. The non-radial components of the electric field limits the resolution of the energy spectrum measurements of the secondary electrons.

In order to rectify this issue, custom hemispheres will be made to ensure that the grids and collector are spherical. This allows the exact size of the grids and collector to be chosen, whereas before they were not. How the collector attaches to the collector ring has also been improved. The hemisphere will have counter-board holes allowing the screw to enter in from the outside of the hemisphere and screw into the baseplate as shown in Fig. 13. The current HGRFA design requires that the hemisphere itself be tapped. Because of the wall thickness of the hemisphere and due to it being constructed using aluminum, the threads have become stripped several times requiring them to be re-drilled and re-tapped. This has caused the screws to bulge the aluminum of the outer-wall, creating an unreliable mounting, as shown in Fig. 14.

E. Wiring

The current wiring of the HGRFA, as shown in Fig. 15 consists of different iterations of improvements which have built upon the instrument. Because of this, the wiring is
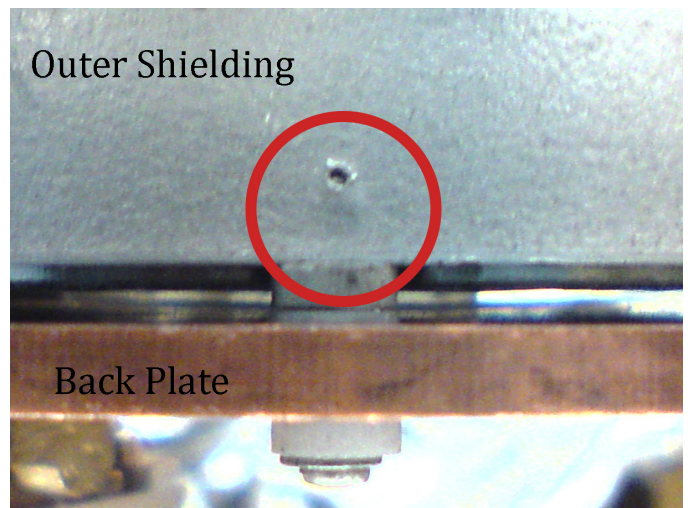
Fig. 14. View of the current HGFRA outer shielding to show the bulging of the aluminum caused by re-tapping stripped threads.

unreliable, un-shielded, and is difficult to disconnect and connect each time the HGRFA must be removed for repairs or improvements. This has led to electrical noise, loss of measurements, shorts between grids, disconnected leads, and shorts to ground.

The new design corrects this by shielding and routing the wiring from the front beam plate, as shown in Fig. 11, to the wire harness as shown in Figs. 12 and 16. The wiring for the grids connects directly to the isolated rings and is then routed down to the wiring harness, as shown in Figs. 12 and 16. At the wiring harness a ceramic quick connector will be made which will allow the easy and quick removal of the HGRFA without needing to change or adjust wiring on the instrument while still maintaining a secure connection that will not disconnect
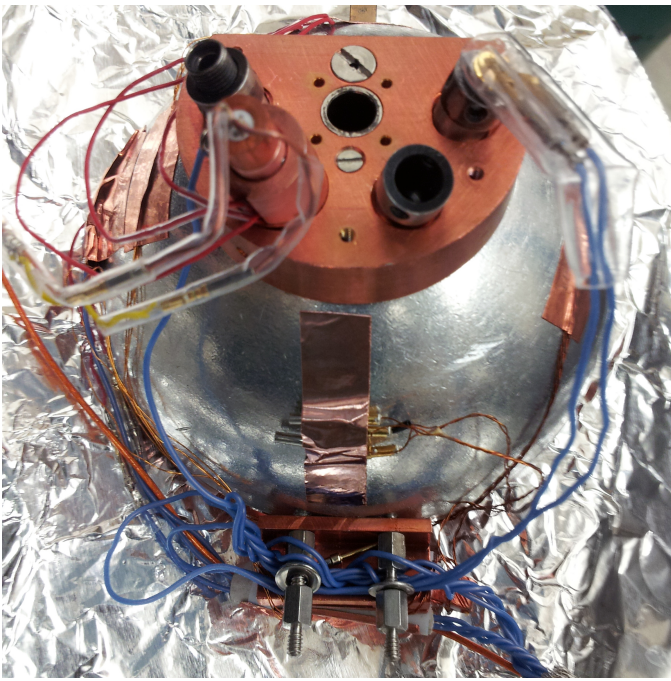
Fig. 15. Current wiring of HGRFA consists of several iterations of modifications.
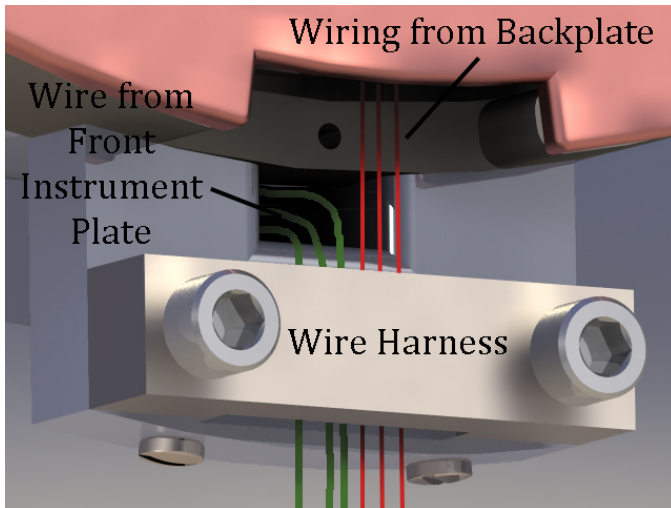

Fig. 16. The wiring from the front panel will run down the wire guide and be held in place by the wire harness. The wiring coming from the insulated rings will come straight down from behind the copper backplate and be held in place by the wire harness.

or short.

F. Center Rod Alignment

Another issue with the current instrumentation deals with the ability to center the electron beam on the sample. To get an accurate profile of the beam, so that the current and spot size are known, the profile has to be measured by a Faraday cup (FC). Because the FC is mounted within one of the sample
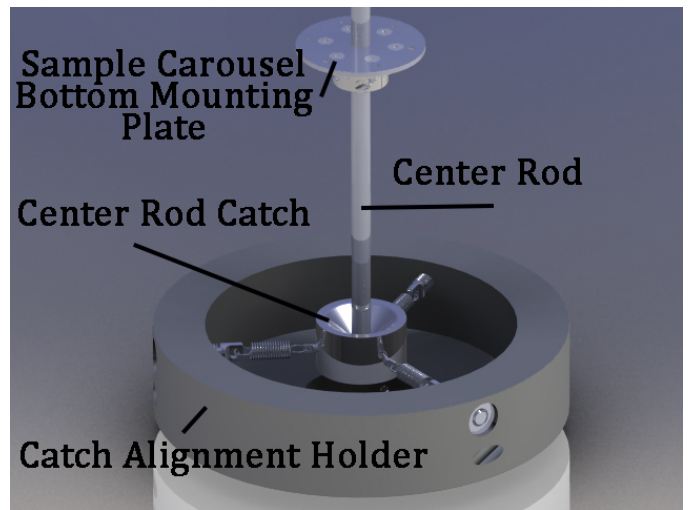

Fig. 17. Design for the Center Rod Catch which will align the carousel with the center of the chamber.

slots, this requires a measurement to first be made with the FC, then the sample carousel is rotated over the desired sample. If the axis of rotation is not aligned with the axis of the chamber, then the sample can be shifted relative to the beam. This changes both the beam current, as well as the beam profile that is hitting the sample. Because the sample carousel is held by a three-axis rod that acts like a pendulum, if the weight on the rod is not balanced then the entire sample carousel can shift. This becomes problematic with use of the HGFRA, since it creates an uneven weight distribution relative to the rod.

In order to fix this problem, a flange with with a 5.1 mm diameter rod affixed, is to be mounted on the bottom of the carousel mounting plate. As the carousel moves up and down the rod will be able to slide in and out of a conical hole. This conical hole, or center rod catch, will then be centered in the chamber by the use of springs, as shown in Fig. 17. This will help align the rod with the chamber axis without requiring that the rod be fixed vertically.

VI. CONCLUSION

By designing and building a new HGRFA, using what USU's MPG has learned from over a decade of measurements, we can increase reliability, reduce noise, ease assembly and disassembly, and open up new measurement possibilities. This instrument will not only allow me to complete the required measurements for my PhD., but it will also allow needed research to be conducted for dynamic secondary electron emission tests, charge storage tests, cathodoluminescence tests, as well as a host of others.

The design itself has taken into consideration everything we have learned from the current instrument as well as future needs as discussed by Christensen [21]. The new instrument will also allow new improvements to be designed and easily added due to its modular design. The measurements and science that will come from this device will not only help our understanding of space craft charging, but it will further

our ability to accurately measure, model and predict the effects of the space environment on novel materials.

REFERENCES

[1] R. Hoffmann, "Electron-induced electron yields of uncharged insulating materials," Master's thesis, Utah State University, Logan, UT, 2010.

[2] G. Wilson and J. R. Dennison, "Approximation of range in materials as a function of incident electron energy," *IEEE Trans. on Plasma Sci.*, vol. 40, no. 2, pp. 305–310, 2012.

[3] A. Starley, G. Wilson, L. Phillipps, and J. Dennison, "Predictive formula for electron penetration depth of diverse materials over large energy ranges," in *14th Spacecraft Charging Technology Conference*, 2016, Conference Proceedings.

[4] L. Reimer, "Scanning electron microscopy: physics of image formation and microanalysis," *Measurement Science and Technology*, vol. 11, p. 1826, 2000.

[5] R. Hoffmann and J. R. Dennison, "Methods to determine total electron-induced electron yields over broad range of conductive and nonconductive materials," *IEEE Trans. on Plasma Sci.*, vol. 40, no. 2, pp. 305–310, 2012.

[6] J. Dennison, J. Christensen, C. Thomson, N. Nickles, R. E. Davies, M. Belhaj, K. Toyoda, A. R. Khan, K. Kawasaki, S. Inoue, I. Montero, M. E. Davila, and L. Olano, "Absolute electron emission calibration: Round robin tests of au and polyimide," in *14th Spacecraft Charging Technology Conference*, 2016, Conference Proceedings.

[7] A. Sim, "A unified theory of charge dynamics in highly insulating materials," PhD Dissertation, Utah State University, Logan, Aug 24, 2010 2012.

[8] H. Wintle, *Conduction processes in polymers*, ser. Engineering Dielectrics: Electrical Properties of Solid Insulating Materials: Molecular Structure and Electrical Behavior. Baltimore, MD: American Society for testing and Materials, 1983, vol. IIA.

[9] J. Fowler, "X-ray induced conductivity in insulating materials," *Proceedings of the Royal Society of London. Series A, Mathematical and Physical Sciences (1934-1990)*, vol. 236, no. 1207, pp. 464–480, 1956.

[10] J. Dennison, J. Gillespie, J. Hodges, R. Hoffmann, J. Abbott, A. Hunt, and R. Spalding, "Radiation induced conductivity of highly-insulating spacecraft materials," in *American Institute of Physics Conference Proceedings Series*, F. D. M. Doyle and B. L., Eds., vol. 1099. Melveille, NY, 2009: American Institute of Physics, 2009, pp. 203–208.

[11] C. Thomson, "Measurements of the secondary electron emission properties of insulators," PhD Dissertation, Utah State University, Logan, UT, March 2004 2004.

[12] H. Bethe and W. Heitler, "On the stopping of fast particles and on the creation of positive electrons," *Proceedings of the Royal Society of London. Series A, Containing Papers of a Mathematical and Physical Character*, vol. 146, no. 856, pp. 83–112, 1934.

[13] J. R. Dennison and A. M. Sim, "Unified density of states based model of electron transport and emission of spacecraft materials," in *12th Spacecraft Charging Techn. Conf.*, Kitakyushu, Japan, May 14-18, 2012 2012.

[14] J. L. Hodges, "In situ measurements of electron beam induced surface voltage of highly resistive materials," Master's thesis, Utah State University, Logan, 2012.

[15] R. Davies and J. Dennison, "Evolution of secondary electron emission characteristics of spacecraft surfaces," *Journal of Spacecraft and Rockets*, vol. 34, no. 4, pp. 571–574, 1997.

[16] W. Chang, J. Dennison, J. Kite, and R. Davies, "Effects of evolving surface contamination on spacecraft charging," in *38th American Institute of Aeronautics and Astronomics Meeting on Aerospace Sciences*, Reno, NV, January, 12 2000, paper received Certificate of Merit by the AIAA Plasmadynamics and Lasers Technical Committee for Best Paper of 2000.

[17] J. Dennison and L. H. Pearson, "Pulsed electro-acoustic (pea) measurements of embedded charge distributions," in *SPIE Optical Engineering+ Applications*. International Society for Optics and Photonics, 2013, pp. 887 612–887 612.

[18] G. Wilson, J. Dennison, A. E. Jensen, and J. Dekany, "Electron energy-dependent charging effects of multilayered dielectric materials," *IEEE Trans. on Plasma Sci.*, vol. 41, no. 12, pp. 3536–3544, 2013.

[19] J. Hodges, "In situ electric field measurements," Masters Thesis, Utah State University, Logan, Utah, 2010.

[20] N. Nickles, "The role of bandgap in the secondary electron emission of small bandgap semiconductors: Studies of graphitic carbon," PhD Dissertation, Utah State University, Logan, UT, August 2002 2002.

[21] J. Christensen, "Electron yield measurements of high-yield low-conductivity dielectric materials," Master's thesis, Utah State University, 2017.

[22] J. Dekany, R. H. Johnson, G. Wilson, A. Evans, and J. R. Dennison, "Ultrahigh vacuum cryostat system for extended low temperature space environment testing," in *12th Spacecraft Charging Techn. Conf.*, Kitakyushu, Japan, May 14-18, 2012 2012.

Gregory Wilson received dual B.S. degrees in physics and mathematics from Utah State University in Logan, UT in 2012. He received an MS in physics from Montana State University in Bozeman, MT in 2015. He is currently a PhD student in physics at Utah State University. He has worked with the Materials Physics Group for four years on electron emission and luminescence studies related to spacecraft charging.